International Journal of Rail Transportation

ISSN: (Print) (Online) Journal homepage: https://www.tandfonline.com/loi/tjrt20

Thermoelectric energy harvesting for wireless onboard rail condition monitoring

Heinrich Foltz, Constantine Tarawneh, Martin Amaro, Sebastian Thomas & Danna Capitanachi Avila

To cite this article: Heinrich Foltz, Constantine Tarawneh, Martin Amaro, Sebastian Thomas & Danna Capitanachi Avila (2023): Thermoelectric energy harvesting for wireless onboard rail condition monitoring, International Journal of Rail Transportation, DOI: 10.1080/23248378.2023.2201247

To link to this article: https://doi.org/10.1080/23248378.2023.2201247

Published online: 10 Apr 2023.

INTERNATIONAL JOURNAL OF RAIL TRANSPORTATION
https://doi.org/10.1080/23248378.2023.2201247

Taylor & Francis
Taylor & Francis Group

Thermoelectric energy harvesting for wireless onboard rail condition monitoring

Heinrich Foltz[a], Constantine Tarawneh[b], Martin Amaro[b], Sebastian Thomas[a] and Danna Capitanachi Avila[b]

[a]Electrical and Computer Engineering Department, University Transportation Center for Railway Safety (UTCRS), University of Texas Rio Grande Valley (UTRGV), Edinburg, TX, USA; [b]Mechanical Engineering Department, University Transportation Center for Railway Safety (UTCRS), University of Texas Rio Grande Valley (UTRGV), Edinburg, TX, USA

ABSTRACT

A thermoelectric energy harvesting device is evaluated to power a bearing health monitoring system. Unlike wayside equipment, the new system is an onboard wireless solution utilizing accelerometer and temperature sensors to assess the bearing condition continuously. The harvesting system consists of two thermoelectric generator modules with aluminium heat sinks, a switching boost converter, a battery management circuit, and a lithium rechargeable battery. The performance of the harvester is validated on an AAR class bearing mounted on a laboratory tester, with load and speed simulating common freight routes of up to 896 miles. The energy harvested varies with operating conditions, and data is presented showing the effect of load and speed. Over a realistic route, the net energy harvested is more than double that needed to indefinitely power a Bluetooth Low Energy sensor. The critical design parameters are the ratio of open-circuit voltage to the temperature difference for the thermoelectric module, and the cold start voltage of the boost converter.

ARTICLE HISTORY
Received 14 September 2022
Revised 24 March 2023
Accepted 3 April 2023

KEYWORDS
Energy harvesting; thermoelectric generators; onboard sensor modules; rolling-stock condition monitoring; bearing and wheel health assessment

1. Introduction

1.1. Wayside bearing health monitoring

Overheated or defective bearings caused 65% of axle/bearing related accidents from 2010 to 2020, according to the Federal Railroad Administration (FRA) [1]. Although there are wayside bearing health monitoring systems in place, they are reactive rather than predictive in nature, only alerting in cases where bearings are nearing failure. The two most widely used bearing health monitoring systems are the Trackside Acoustic Detection System (TADS™) and the Hot-Box Detector (HBD). The TADS™ uses an array of microphones set up along both sides of the rail tracks at specific locations to assess bearing defects under nominal operating speeds [2]. Although this system is proficient in detecting bearings with spalls (defects) on their outer ring raceways, it is not as efficient in detecting bearings with spalls on their inner ring raceways, and there are less than 30 TADS™ sites in the USA and Canada [3], which means that many bearings can go through their entire service life without passing through one of these sites. The wayside HBD uses non-contact Infrared (IR) sensors to obtain the temperatures of the bearings, axles, and brakes to gauge component health. An alarm is triggered if the temperature difference

CONTACT Constantine Tarawneh constantine.tarawneh@utrgv.edu Mechanical Engineering Department, University Transportation Center for Railway Safety (UTCRS), University of Texas Rio Grande Valley (UTRGV), Edinburg TX 78539, USA

between the bearing surface and ambient reaches a predetermined threshold set by the Association of American Railroads (AAR). Although HBDs are more prevalent than other forms of bearing condition monitoring systems, with over 6,000 units installed throughout the United States, they have their own set of drawbacks. HBDs have exhibited inconsistent results by under- or over-predicting bearing operating temperatures. This has led to HBDs flagging false positives and, in worst-case scenarios, missing defective bearings that eventually failed, causing costly train derailments [4].

1.2. Wireless onboard monitoring

Onboard systems have two major advantages relative to wayside systems. First, they allow continuous monitoring, so that rapidly deteriorating bearings can be detected immediately. Second, they allow the use of more accurate direct contact temperature and vibration sensors. The improved accuracy allows early detection and classification of small defects, which are not yet large enough to require bearing replacement. Early detection allows bearing health monitoring to be predictive rather than reactive, which in turn enables scheduled preventive maintenance and averts the need for emergency field replacements.

The team at the University Transportation Center for Railway Safety (UTCRS) has developed a prototype wireless onboard condition monitoring module that can continuously gauge bearing health and identify defective bearings in the early stages of defect propagation [5]. The module is installed on the outboard surface of the bearing adapter and communicates wirelessly. It contains a temperature sensor, a high-accuracy analogue accelerometer, and a microcontroller with Bluetooth LE™ capability. A single non-rechargeable 3.7 V lithium cell, 14500 size (physical dimensions equivalent to AA battery), can operate the module for 3 months in the 'always awake' mode. With the use of controlled sleep periods, it is estimated that the lifetime can be extended to 2 years without recharging.

However, battery replacement, even at two-year intervals, would represent significant labour costs. A desirable solution would eliminate battery replacement entirely through energy harvesting.

1.3. Energy harvesting methods

A wide variety of energy harvesting techniques are available including vibration (electromechanical, piezoelectric, or magnetostrictive), photovoltaic, and thermoelectric. An extensive review of vibration- or motion-based harvesting for rail tracks and cars was given in [6]. Two interesting examples are a levitating magnet harvester [7] and an inverted pendulum [8]. Both systems are mounted on the track and harvest energy from passing trains to power networked sensors and actuators.

For the application considered here, where the energy harvesting must be close to the railcar suspension, it is desirable for the energy harvester to be compact and robust. Electromechanical methods generate significant power but are relatively large and have moving parts. Piezoelectrics are small and have no macroscopic motion; however, the power density is low except near particular resonant frequencies. Magnetostrictive materials with suitable magnetostrictive coefficients (such as Terfenol-D) are costly and tend to fracture when subjected to cyclic loading at the strain levels needed for significant power output.

Photovoltaics are well-known, low-cost, and highly effective when clean, undamaged, and properly positioned, but are subject to surface fouling, impact, and shading when mounted on a railcar bogie frame or bearing adapter.

For mounting directly on a bearing adapter, thermoelectric generators (TEGs) have the potential to meet the requirements of being small, having no moving parts, and being relatively insensitive to temperature. On first impression, one might believe that performance would be highly dependent on ambient temperature, but as discussed in Section 2.2, this is not the case.

Thermoelectric generation is an established technology [9] for general harvesting applications and has been evaluated specifically for rail applications. In [10], a thermoelectric generator using the difference in temperature between sun-heated rail and cooler underlayment produced up to 317-mW of power for wayside sensors and actuators.

The work most closely related to that presented here was a study of TEGs mounted to high-speed passenger train bearing adapters [11]. In the experiment, it was found that a single TEG device had an available power of up to 20-mW on a train moving at 300 km/h. The experiment provided valuable confirmation of feasibility and design guidelines for cold-side heat-sinking. However, there was no systematic study of the variation of performance with loading and speed, and the onboard test measured open-circuit performance without conversion electronics or actual loading.

For this project, a complete energy harvesting device was tested for rail freight applications where speeds are much lower, and loading is more variable. The effects of changes in railcar load and speed were determined under conditions that included power conversion electronics, batteries with associated charge control, and an operating wireless system. It should be emphasized that the individual system components are commercially available; the primary objective is to quantify performance variations caused by usage on a railcar bearing adapter.

In Section 2, basic design considerations are discussed along with preliminary off-board testing to establish the baseline performance for the TEG under ideal hot-plate conditions. Section 3 describes the main experiment, conducted on a four-bearing tester, and Section 4 presents an analysis of the results.

2. Design considerations

2.1. TEG placement

Figure 1 shows the arrangement of TEG modules used. In typical thermoelectric generation systems, the strategy is to insulate the hot side mass in order to force heat to exit only through the TEG modules. This is *not* an acceptable strategy for this application since it would increase the overall thermal resistance from bearing to ambient and thus make the bearing run hotter. Furthermore, it is not necessary, since the heat generated in the bearing exceeds the power required to operate wireless instrumentation by several orders of magnitude. Railroad bearings typically generate 200–600 Watts of heat depending on speed, load, and bearing condition [12], while the wireless system used here requires less than 3-mW average power.

The modules in this system cover less than 6% of the adapter surface that is exposed to air and thus have negligible effect on the adapter's ability to self-cool. Two modules are used, one mounted on the leading face of the adapter and one mounted on the trailing face. This arrangement ensures

Figure 1. TEG and heat sinks mounted on the bearing adapter. The associated harvesting electronics and instrumentation were mounted offboard to allow real-time performance monitoring.

Table 1. Key parameters for thermoelectric generator module.

Parameter	Value
Part Number	Tecteg TEG2-126DLT
Dimensions	40mm × 40mm × 5.14mm[a]
Number of Junction Pairs	~120[c]
Thermal Resistance R_{mod}	3.3 K/W[b]
V_{oc} /ΔT_{mod}	0.05 V/K[b]
Thevenin Resistance R_{th}	4.2 Δ[a], 5.6 Δ[c]

[a]Datasheet value [16]. [b]Computed from datasheet information. [c]Observed.

that at least one module's heat sink will receive adequate airflow when the railcar is in motion, regardless of direction of travel.

2.2. Effect of ambient temperature

The performance of the TEG system, to a good approximation, is expected to be independent of ambient temperature. The adapter itself acts as a lumped thermal capacitance body; experimentally validated finite element simulations show that the temperature differs by less than 3°C throughout the adapter volume [13]. For a given load, speed, and condition, the internal bearing friction creates a constant power source, rather than a constant temperature source. For a given airflow, the thermal resistance of the adapter to air is nearly independent of temperature. The time constant for the system is in the range of 30–60 minutes. Therefore, after an initial transient period, the system operates with a temperature difference $\Delta T_{aa} = T_{adp} - T_{amb}$ (where T_{adp} is the adapter temperature, which is dependent on bearing condition, load, and speed but not on ambient temperature (T_{amb}). The power available from a given TEG module is determined almost entirely by the temperature differential between the faces of the module, ΔT_{mod}, which is less than ΔT_{aa} by the ratio:

$$\frac{\Delta T_{mod}}{\Delta T_{aa}} = \frac{R_{mod}}{R_{a,mod}+R_{mod}+R_{mod,h}+R_{h,amb}} \tag{1}$$

where R_{mod} is the thermal resistance of the TEG module, and the other resistances are from the adapter to the module ($R_{a,mod}$), the module to the heat sink ($R_{mod,h}$), and the heat sink to ambient ($R_{h,amb}$). These resistances as well as ΔT_{aa} are nearly independent of ambient temperature; however, $R_{h,amb}$ will differ for the leading and trailing heat sinks. For the system described here, we have found that $\Delta T_{mod}/\Delta T_{aa} \approx 0.41$ averaged over the leading and trailing modules, using directly measured ΔT_{aa}, and ΔT_{mod} inferred from the observed open-circuit voltage and the module specifications (see Table 1).

2.3. Thermoelectric module and heat sink selection

In this application, it is critical to be able to harvest energy at low-temperature differentials (less than $\Delta T_{aa} = 10$ K). Modules should be optimized for high open-circuit voltage V_{oc} at low temperature differential. This in turn requires (a) junctions doped for a high Seebeck coefficient and (b) a large number of junctions arranged electrically in series but thermally in parallel. The best bismuth telluride junctions have a coefficient of less than 500 ΔV/K [14], and commercial harvesting electronics typically need 60 mV or more to self-start [15]. This implies that >100 junctions are needed to self-start when $\Delta T_{mod} = 1$ K (K = Kelvin).

The TEGs used for the data presented here are the Tecteg TEG2-126LDT. The intended application of these modules was harvesting body heat [16], and they can generate useful amounts of power at single digit temperature differentials. Table 1 shows the key parameters for a single module. Two modules (leading and trailing) are used in the series.

The heat sinks used are made of 6063-T5 aluminium, with overall dimensions 40 × 40 × 20 mm, 11 fins, and a thermal resistance of 1.5 K/W with forced air convection at 6 m/s. It should be noted that a larger sink with lower $R_{h,amb}$ would give better performance; however, the dimensions are constrained by the TEG size in two dimensions and the limits on acceptable protrusion from the adapter in the third dimension.

The TEGs and heat sinks were mounted to the adapter using a thermal adhesive with thermal conductivity value of 0.9 W/m·K. Taking into account that the trailing heat sink has a somewhat higher resistance due to reduced airflow, and additional resistances in the adhesive and the adapter itself, the total thermal resistance is sufficient to account for the observed ratio $\Delta T_{mod}/\Delta T_{aa}$ discussed in Section 2.2.

It is useful to have a formula for the expected power available prior to any boost conversion or charge control. Although the thermoelectric potential is not a perfectly linear function of ΔT_{mod}, performance curves in [16] show that for the range of temperature difference expected on a viable bearing, ΔT_{mod}<60K, less than a few percent error is incurred by assuming V_{oc} is linearly dependent on ΔT_{mod} with a fixed coefficient.

Likewise, the electrical load line for a TEG is nearly linear and is accurately modelled by V_{oc} and a Thevenin resistance R_{th}. The Thevenin resistance itself may be weakly dependent on temperature and heat flow; however, comparison of observed load lines taken at different temperatures within the operating range showed that any variation in R_{th} was less than the measurement resolution.

The available electrical power from an electrical device modelled by its Thevenin equivalent is given by $P_{av} = V_{oc}^2/(4R_{th})$, obtained at the *maximum power point* (MPP) given by V=V_{oc} /2, I=V_{oc} /(2R_{th}). One then substitutes $V_{oc} = k_1\ \Delta T_{mod}$, where the value for $k_1 = V_{oc}\ /\Delta T_{mod} = 0.05$ V/K is determined graphically from the starting slope of the datasheet performance curves. The value of $R_{th} = 5.6\ \Delta$ was obtained by direct measurement of the load line with multiple loads and curve-fitting. As stated above, this was done at multiple temperatures with identical results. Thus, the expected available power is

$$P_{av} = 2.2 \times 10^{-4}(\Delta T_{mod})^2 \tag{2}$$

It is not feasible to directly measure ΔT_{mod} during operation since the plates of the TEG are both completely covered; however, ΔT_{aa} is easily monitored. Therefore, we use the value of $\Delta T_{mod}/\Delta T_{aa}$ ≈0.41 from Section 2.2. This ratio was determined experimentally by operating at a known ΔT_{aa}, measuring V_{oc}, and then inferring ΔT_{mod} using the constant k_1. Since the two modules may not be at identical temperatures, an average was taken over data collected from several simulated runs.

Then, substituting $\Delta T_{mod} = 0.41$, ΔT_{aa} yields:

$$P_{av} = 3.7 \times 10^{-5}(\Delta T_{aa})^2 \tag{3}$$

Equation (3) gives the expected available power for *two* TEG modules in series for this particular adapter and heat sink combination. The actual power harvested and stored will be less due to (a) operation not exactly at the MPP, and (b) the imperfect efficiency of the boost converter and charge control electronics. Note that the MPP is a function of temperature. Ideally, it needs to be dynamically controlled as the bearing adapter heats or cools.

2.4. Voltage boost and battery charge management

The TEG modules generate a variable output voltage unsuitable for direct battery charging. Both voltage boost and battery charge management are necessary, with special considerations for low ΔT harvesting. Figure 2 shows a wiring diagram.

To be able to recover from a complete battery discharge, it is required that the boost converter be capable of cold starting; that is, restart operation using only the TEG output. The results of our

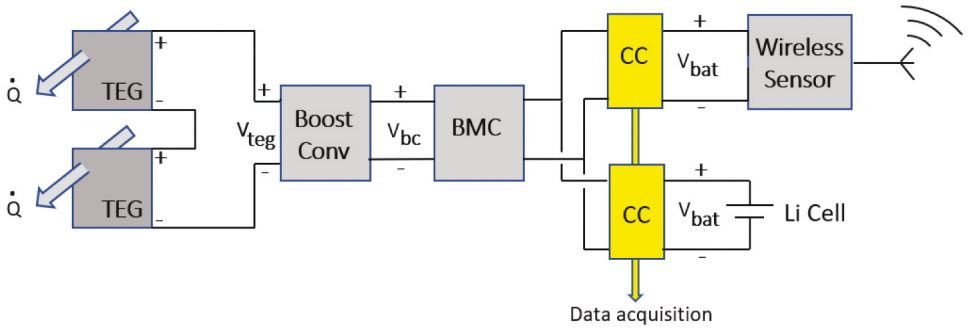

Figure 2. Wiring diagram of energy harvesting system, showing thermoelectric generator (TEG) modules in series, boost converter, battery management (BMC), coulomb counters (CC), lithium storage battery, and wireless sensor [5] to be powered. The coulomb counters and data acquisition are only included for test purposes and are separately powered.

experiments show that a key specification is the minimum cold start voltage (V_{cs}). Commercial off-the-shelf solutions can have V_{cs} as low as 60-mV, but at some cost and added complexity.

After the boost converter, battery management circuitry (BMC) ensures that the battery is not damaged. The TEG is not capable of even approaching the maximum charge rate for a lithium cell; however, the cell can be damaged by continuing to charge after it has reached capacity even at low charge rates. The BMC ensures cut-off when full capacity is reached. Prior to cut-off, the ideal charge current is that which will operate the TEG, which varies with ΔT_{mod}. The ideal solution is an MPP tracking circuit; however, useful amounts of energy can be harvested at points away from the MPP.

Two different circuits were evaluated. The first one used separate, low-cost, generic boost converter and charge management modules and does not directly track MPP. The boost converter (Songhe, ASIN B07YYMNJ1J) has a nominal output of V_{bc} = 5-VDC, slightly higher than is needed for charging, and is observed to cold start when $V_{teg} > V_{cs}$≈0.9 V. It is followed by a TP4056 conventional charge management chip [17]. Figure 3 shows the different operating regions. The TP4056 target charge current for the constant current phase is resistor programmed to a compromise value (32 mA in the figure) that is close to the MPP at the highest temperature differences expected (50–60 K), in order to rapidly gain charge. At lower but significant

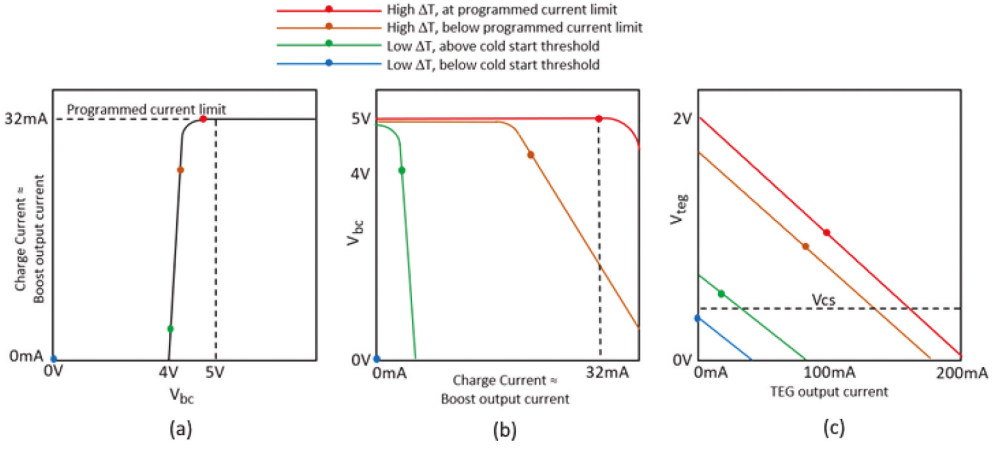

Figure 3. Conceptual operation of the harvesting electronics. The graph at (a) shows the charge current versus input voltage for the charge management (BMC). The graphs at (b) and (c) show the output characteristics for the boost converter and TEG, respectively, which are temperature dependent. The colored dots show the operating points at different temperatures.

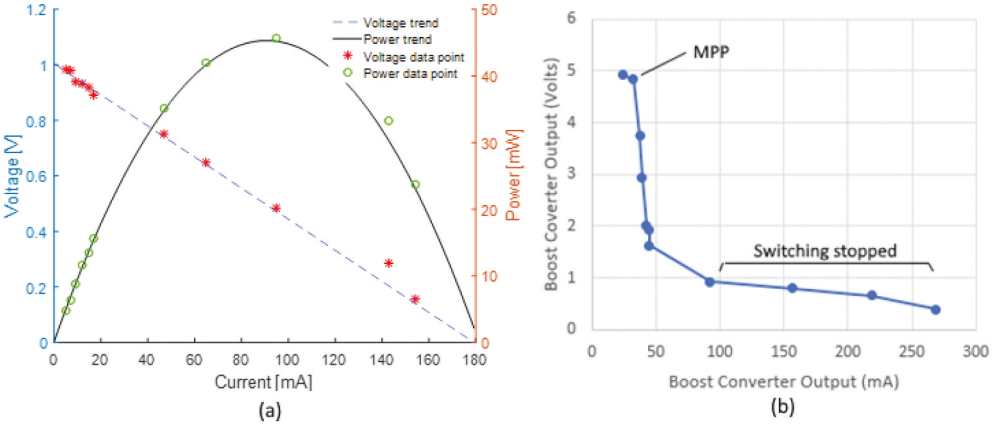

Figure 4. (A) Experimental performance of a single TEG2-126LDT (40 × 40 mm) alone. Estimated ΔT_{mod} = 20 K. (b) Typical performance of boost converter powered by two TEGs in series. Estimated ΔT_{mod} = 30 K. At the MPP, the output power is 157 Mw, compared to estimated available input power P_{av} of 198 Mw.

temperature differences, the BMC operates short of its programmed charge current, and the boost converter outputs slightly below its nominal value, that is, V_{bc}<5 V. Due to the sharp slope of the BMC charge with respect to V_{bc}, there is a reasonably wide range of ΔT_{mod} and V_{teg} for which the system can provide charge. However, when $V_{teg} < V_{cs}$, the system stops completely.

The second system tested (E-peas AEM20940 [15]) is specifically designed for TEG applications. It integrates, in one chip, the functions of the boost converter and BMC blocks in Figure 2. The MPP tracking algorithm adjusts the charge current such that the TEG operates with an output voltage $V=V_{oc}/2$, which is the theoretical MPP at low temperature differential. With the aid of an external discrete cold start circuit, V_{cs} can be as low as 60 mV, so it is expected that the second system will be able to charge at much lower temperature differentials.

2.5. Off-bearing testing and optimization

Prior to testing on a railroad adapter, a set of preliminary measurements were made using a hot plate, a single TEG, a large heat sink with forced air cooling, and a series of different load resistors. The purpose of these measurements was to verify the TEG characteristics. It should be noted that it is difficult to reproduce the precise operating conditions used to obtain the datasheet specifications and that IR temperature measurements of the heat sink and hot plate only allow an estimate of ΔT_{mod} Nevertheless, the TEG output is very close to an ideal Thevenin characteristic. A typical curve is shown in Figure 4 (Left). For this example, V_{oc} = 1.0-V, I_{sc} = 180 mA, R_{th} = 5.55 Δ and P = 45.0 mW at the MPP.

For the first version of the harvesting electronics, which uses separate boost conversion and BMC, it was necessary to optimize the charge rate programmed into the BMC. To do this, the output characteristics of the TEG/boost combination are needed. Two TEG modules operated at a high ΔT_{mod} (>30 K) were used in the series as input to the boost converter, and a series of different resistive loads were tested. A boost converter's MPP is at the knee where voltage regulation (in this case at 5 V) is lost. At high load currents, the converter ceases switching and essentially passes through the TEG voltage and current. As shown in Figure 4 (right), the knee for this test was at 32-mA and 4.9 V, leading to a delivered power of 157 mW. This can be compared to 198 mW available at the boost converter input, as estimated from Equation (3). Since the BMC has a very low quiescent (overhead) current, the boost converter output current almost equals the battery charge current; therefore, the charge current was programmed to 32

mA. The second version of the harvesting electronics automatically tracks the MPP, and optimization is not required.

Although hot plate experiments can give a rough indication of the expected performance, an actual adapter with a running bearing as the heat source has different thermal resistances and time constants. In the next section, we describe a laboratory setup that reproduces realistic rail service operating conditions.

3. Experimental setup and procedures

3.1. Bearing tester and instrumentation

To verify the performance of the entire system, a prototype unit was mounted on a UTCRS-owned dynamic bearing test rig. This tester, depicted in Figure 5, is designed to reproduce the operating conditions of AAR class K (6½‘×9’), class F (6½‘×12’), class G (7‘×12’), and class E (6‘×11’) tapered roller bearings in a temperature-controlled environmental chamber with controlled wind speed. It is equipped with a hydraulic cylinder capable of applying loads of up to 150% of the maximum AAR rated load for class F and K bearings (153 kN or 34.4 kips per bearing) Feedback-based load controllers are used to maintain a constant applied load on the bearings and automatically adjust the load to counteract any variations due to thermal expansion and contraction of the hydraulic oil. The axle is driven by a 22 kW (30 hp) motor, with variable frequency drive allowing speeds of up to 137 km/h (85 mph). Industrial fans are set perpendicular to the tester to provide passive air cooling (6 m/s or 13.4 mph) to the bearings.

The tester can accommodate four bearings pressed onto a test axle. The two middle positions are top-loaded, while the two outer positions are bottom-loaded. The middle positions were used for this study since they have more realistic loading and airflow patterns.

In this study, the bearings were subjected to two loading conditions, which include 17% railcar load (26 kN or 5.85 kips per bearing), representing an empty railcar, and 100% railcar load (153 kN or 34.4 kip per bearing), replicating a fully loaded railcar. The air-conditioning unit inside the environmental chamber was set to 21°C (70°F). Four class K bearings were mounted on the text

Figure 5. Four bearing dynamic test rig housed in an environmental chamber capable of producing ambient temperatures as low as −40°C and as high as 60°C.

axle. Three were control (defect-free) bearings and one was a defective bearing containing a cup (outer ring) spall of approximately 12.9 cm^2 (2 in^2) area. The outer positions on the axle were defect-free bearings, the middle positions had one defect-free (healthy) and one defective bearing. An energy harvesting device was placed in each of the two middle bearings. Prior to each run, the battery was discharged to 850 mAh or 77% SoC (state of charge).

During the experiment, a data acquisition system continuously monitored ambient and adapter temperatures using K-type thermocouples along with battery voltage. The current was monitored with two hardwired, separately powered coulomb counters (yellow blocks marked CC in Figure 2) inserted between the BMC and the battery, and between the BMC and the wireless monitoring device. Coulomb counters are integrating type devices that output a pulse and reset when a set amount of charge has passed. This type of measurement is more suitable than direct current measurement since the wireless device draws current with a semi-random pulsed waveform, and since the wireless device current subtracts from the total BMC output current, the battery current is semi-random as well. The CC output pulses are counted by a separate microcontroller that displays total charge accumulated.

3.2. Routes simulated

A set of test plans were developed to replicate the operating conditions seen in common freight routes. The first route selected was between Billings, MT, and Council Bluffs, IA. This route is commonly used to transport coal and is approximately 896.4 miles in length and takes about 15.76 hours to complete. The second route selected was between Fairfield, AL, and New Orleans, LA. This route simulates a railcar transporting cargo from a steel mill to a shipyard. It runs 427.2 miles in length and takes approximately 11.59 hours to complete. The speeds in the test plans were estimated by using the urban density of a corresponding area along with existing railroad speed data [18]. Figures 6 and Figure 7 show the maps for these two routes. Tables 2 and 3 list the cities on these routes, along with the distance, speed, and elapsed time for each segment.

The two routes were selected to test more favourable (higher speed) and less favourable (lower speed) scenarios for energy harvesting. Route 1 is primarily rural and allows higher

Figure 6. Map of Route 1 (Council Bluffs, IA, to Billings, MT) [19].

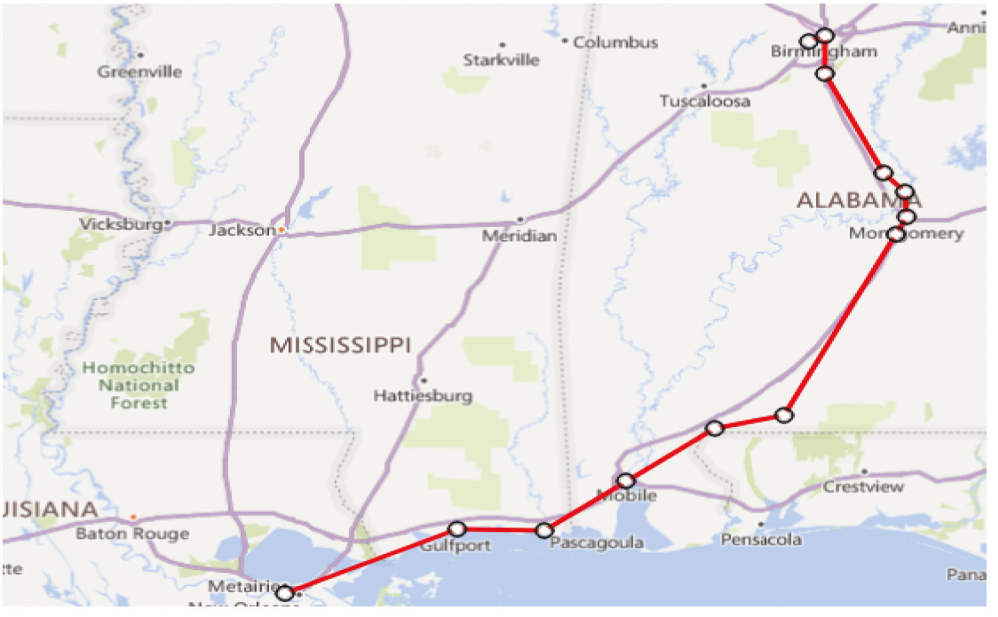

Figure 7. Map of Route 2 (Fairfield, AL – New Orleans, LA) [19].

Table 2. Distance and speed limits of Route 1 (Council Bluffs, IA, to Billings, MT).

Segment	Distance [mi]	Speed [mph]	Time [h]
1. Council Bluffs - Gretna	24.3	25	0.97
2. Gretna - Ashland	10.5	35	0.30
3. Ashland - Moorcroft	589.8	60	9.83
4. Moorcroft - Rozet	13.2	53	0.25
5. Rozet - Sheridan	18.0	45	0.40
6. Sheridan - Billings	240.6	60	4.01
Cumulative	**896.4**	**56.9 avg**	**15.76**

Table 3. Distance and speed limits of Route 2 (Fairfield, AL, to New Orleans, LA).

Segment	Distance [mi]	Speed [mph]	Time [h]
1. Fairfield - Birmingham	11.25	25	0.45
2. Birmingham - Rollins	73.50	35	2.10
3. Rollins - Montgomery	23.65	55	0.43
4. Montgomery - McGehees	9.0	45	0.20
5. McGehees - Brewton	96.6	60	1.61
6. Brewton - Atmore	27.5	55	0.50
7. Atmore - Mobile	45.0	45	1.00
8. Mobile - Gulfport	73.5	35	2.10
9. Gulfport – New Orleans	67.5	25	2.70
Cumulative	**427.5**	**38.54 avg**	**11.09**

speeds for longer periods of time, while Route 2 involves more urban areas that require lower speeds for shorter periods of time. Each route was run in two parts as a round-trip. The first part simulated the railcar travelling fully loaded to its destination, while the second part simulated the railcar returning empty to its point of origin. The accumulated charge for each segment was measured.

Table 4. Summary of laboratory test runs.

Run #	Route/ Direction	Load	Bearing Condition	Wireless Device	Circuit Used
1	1/→	100%	Healthy	None	High V_{cs}
2	1/→	100%	Cone Spall	None	High V_{cs}
3	1/←	17%	Healthy	None	High V_{cs}
4	1/←	17%	Cone Spall	None	High V_{cs}
5	2/→	100%	Healthy	1 sec	High V_{cs}
6	2/→	100%	Cup Spall	1 sec	High V_{cs}
7	2/←	17%	Healthy	1 sec	High V_{cs}
8	2/←	17%	Cup Spall	1 sec	High V_{cs}
9	1/→	100%	Healthy	4 sec	High V_{cs}
10	1/→	100%	Cup Spall	4 sec	High V_{cs}
11	1/←	17%	Healthy	4 sec	High V_{cs}
12	1/←	17%	Cup Spall	4 sec	High V_{cs}
13	2/→	100%	Healthy	4 sec	High V_{cs}
14	2/→	100%	Cup Spall	4 sec	High V_{cs}
15	2/←	17%	Healthy	4 sec	High V_{cs}
16	2/←	17%	Cup Spall	4 sec	High V_{cs}
17	2/←	17%	Cup Spall	None	Low V_{cs}
18	2/→	100%	Cup Spall	None	Low V_{cs}

3.3. Test runs

A total of 18 one-way routes (nine equivalent round trips) were run, as summarized in Table 4. The total time was 237 hours covering an equivalent travel distance of 11,446 miles (18,421 km). Parameters varied included: (a) speed, according to the tables in the previous section, (b) load at 17% or 100%, (c) healthy or defective bearings, (d) wireless device either absent, run with a 1-second algorithm, or run with a 4-second algorithm, and (e) two versions of the harvesting electronics, either the separate modules with high cold start voltage (V_{cs}) or the MPP circuit with low cold start voltage.

There were two motivations for running with and without wireless devices in operation. One was to determine if the rapidly time varying current drawn by the device would affect the charging circuit performance. The second was to directly demonstrate that the system can produce a net gain in charge. When used, the wireless device was set to take vibration data every 10 minutes. Either 1-second (5200 time samples) or 4-second (20800 time samples) were taken. The vibration spectra are not relevant to this paper; however, the number of samples processed and transmitted can affect the power consumption. It should be noted that the processor and Bluetooth LE transceiver remain continuously active to receive requests from the data hub.

Due to a unipolar limitation in the coulomb counters used with the first (high V_{cs}) circuit, and the fact that the circuit only starts when fairly high amounts of power are available, an assumption was made in the data collection: the boost circuit was started when the battery was charging, and off when it was not charging. For the low V_{cs} circuit, this is not true, since it can be on at power levels that contribute to powering the wireless device but still require some battery discharge. In these cases, bipolar readings were used.

4. Results

4.1. Example data

Results from two runs (#5 and #7) are shown in detail in Tables 5 and 6. Together, they represent one round-trip, outgoing loaded and returning empty, using the first harvesting circuit, which has a high (V_{cs}≈0.9-V) cold start threshold voltage. The column labelled 'Charge Produced by BMC' is the sum of the 'Charge into Battery' and 'Charge into Wireless'. A few significant trends emerge immediately:

Table 5. Results for Run #5. Route 2, 100% railcar load, healthy bearing, wireless set to one-second of data every 10 minutes. Battery voltage rose from 3.84 to 3.87 V during experiment.

Time [h]	Speed [mph]	Avg. T_{amb} [°C]	Avg. T_{adp} [°C]	ΔT_{aa} [°C]	Charge Produced by BMC [mAh]	Charge into Battery [mAh]	Charge into Wireless [mAh]	Avg. Power Generated [mW]	Avg. Power Wireless [mW]
0.45	25	20	33	14	0.00	−0.17	0.17	0.0	1.5
2.1	35	19	36	17	0.00	−1.20	1.20	0.0	2.2
0.43	55	17	39	21	0.51	0.34	0.17	4.6	1.5
0.2	45	20	43	23	0.51	0.34	0.17	9.8	3.3
1.61	60	18	48	30	10.58	9.05	1.53	25.4	3.7
0.5	55	19	50	31	3.24	3.07	0.17	25.1	1.3
1	45	18	46	28	5.64	4.78	0.86	21.8	3.3
2.1	35	18	39	20	3.24	2.05	1.19	6.0	2.2
2.7	25	19	34	15	0.00	−1.54	1.54	0.0	2.2
Total:					23.72	16.72	7.00		

Table 6. Results for Run #7. Route 2, 17% railcar load, healthy bearing, wireless set to one-second of data every 10 minutes. Battery voltage was 3.86 V throughout the experiment.

Time [h]	Speed [mph]	Avg. T_{amb} [°C]	Avg. T_{adp} [°C]	ΔT_{aa} [°C]	Charge Produced by BMC [mAh]	Charge into Battery [mAh]	Charge into Wireless [mAh]	Avg. Power Generated [mW]	Avg. Power Wireless [mW]
2.7	25	19	26	7	0.00	−1.37	1.37	0.0	2.0
2.1	35	19	27	9	0.00	−1.19	1.19	0.0	2.2
1	45	19	29	10	0.00	−0.51	0.51	0.0	2.0
0.5	55	18	31	13	0.00	−0.34	0.34	0.0	2.6
1.61	60	18	34	15	0.00	−0.86	0.86	0.0	2.1
0.2	45	19	35	16	0.00	−0.17	0.17	0.0	3.3
0.43	55	18	34	16	0.00	−0.17	0.17	0.0	1.5
2.1	35	19	31	13	0.00	−1.19	1.19	0.0	2.2
0.45	25	18	29	11	0.00	−0.34	0.34	0.0	2.9
Total:					0.00	−6.14	6.14		

- For this configuration of the electronics, harvesting cuts off completely when ΔT_{aa} is at 17°C (17 K) or less. This agrees well with the TEG module coefficient (0.05 V/K for two modules) and V_{cs} = 0.9-V, which predicts operation will not start below an 18°C (18 K) temperature differential.
- As expected, once the circuit is above the threshold, the average power increases rapidly with ΔT_{aa}.
- The temperature differential depends strongly on load and speed. As a result, no measurable harvesting took place at 17% load, regardless of speed, and at 100% load, harvesting typically started at 35 mph (56 kph).
- Averaged over an entire round-trip, there was a net gain of charge (16.72 – 6.14 = 10.58 mAh) in the battery even while continuously powering the wireless device.

Similar tables were generated for all the runs as part of the study in [20]. In the interest of brevity, they will not be presented here. In general, a similar behaviour was observed: a cut-off threshold at low ΔT_{aa}, a faster than linear increase in power with temperature above the threshold, little or no harvesting when unloaded and a net gain (more energy generated than consumed) when loaded plus unloaded segments were combined.

4.2. Temperature differential vs. speed and load

The variation of the bearing temperature with speed and load has been extensively studied [21]. To confirm that our experiment aligns with expectations, the data from runs 1, 3, 5, …15 were

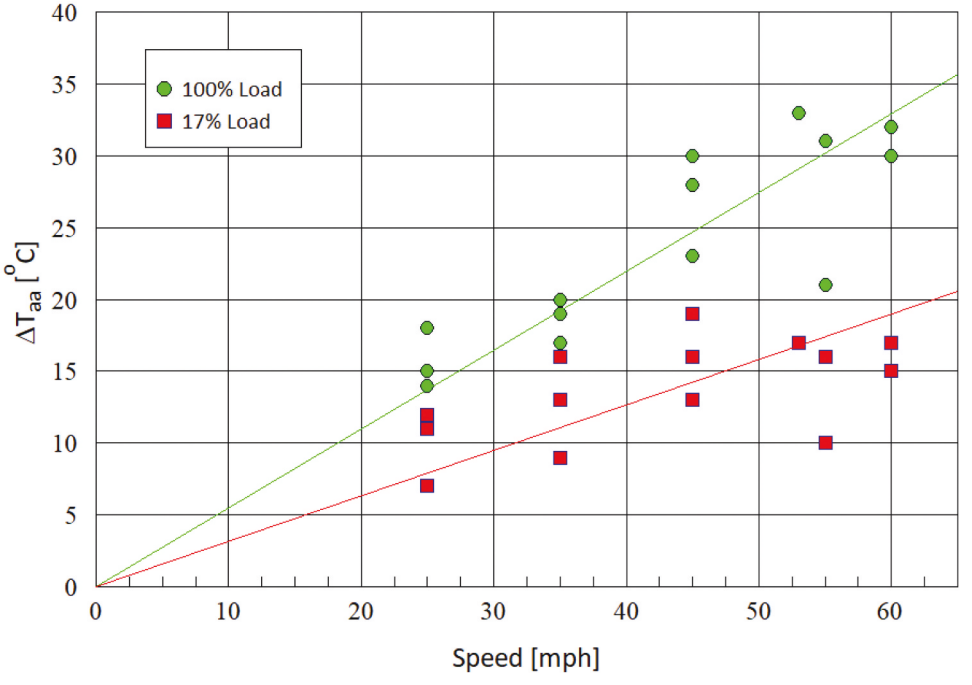

Figure 8. Variation of observed temperature differentials with speed and load for a healthy bearing.

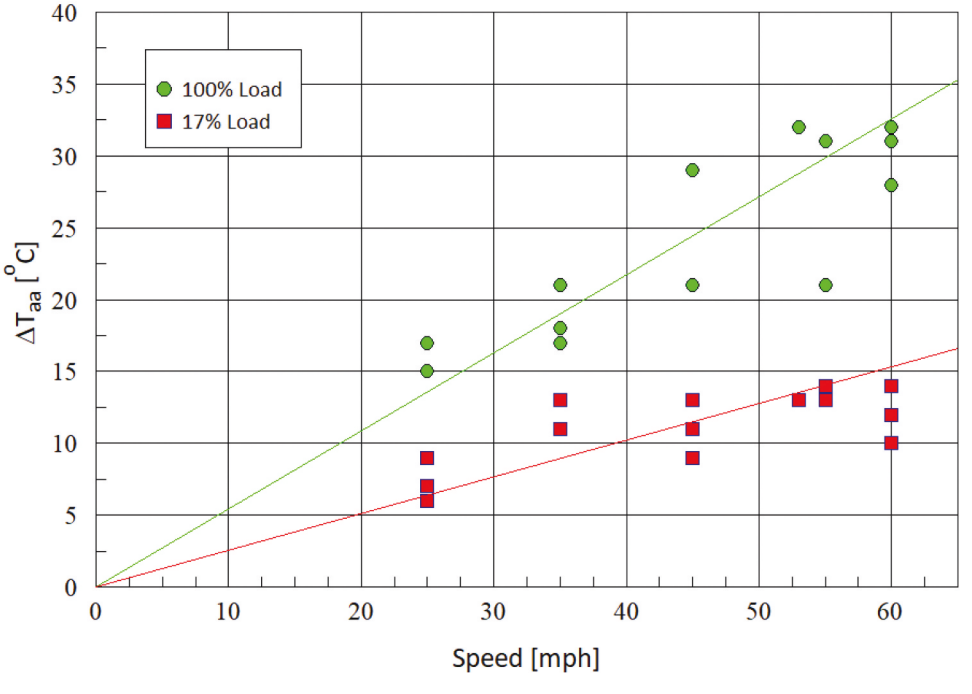

Figure 9. Variation of observed temperature differentials with speed and load for a bearing with a 12.9 cm^2 (2 in^2) cup spall.

combined since they all used the same healthy bearing. Figure 8 shows that temperature increases approximately linearly with speed, and that the rise is considerably steeper for a fully loaded car than for an unloaded car. Figure 9 shows the same analysis for a bearing with a cup spall, from runs 2, 4, 6, . . .16. One expects severely degraded bearings to have higher temperature differentials; however, that is not necessarily the case for smaller defects like the one tested here [21]. A small cup spall can act as a reservoir for lubricant, counteracting increased friction due to the spall itself. In this experiment, little difference was seen between the healthy and defective bearings.

4.3. Harvesting performance vs. Temperature

From Equation (3), it is expected that the power available will be directly correlated with the square of the temperature differential. The power actually delivered to the battery and/or wireless will be somewhat less due to losses in the conversion and charge electronics. Figure 10 shows the observed relationship. Each datapoint represents the average power and average temperature over one segment of one run. The data in general aligns with expectations. One should note the behaviour of the high V_{cs} circuit (green points in Figure 10) at low temperatures. If the temperature during a segment never reaches the 17°C threshold, the power generated is zero. The low V_{cs} circuit, in contrast, produces non-zero power at every combination of speed and load tested.

Since the relationship is nonlinear and the average is being used, points can occasionally exceed the maximum. For example, an initial segment over which the temperature increased linearly from 0 to 20°C (0 to 20 K) would collect so much more power when close to 20°C that the average is higher than expected for 10°C. This effect also accounts for some of the non-zero points in the high V_{cs} circuit at low-temperature differentials.

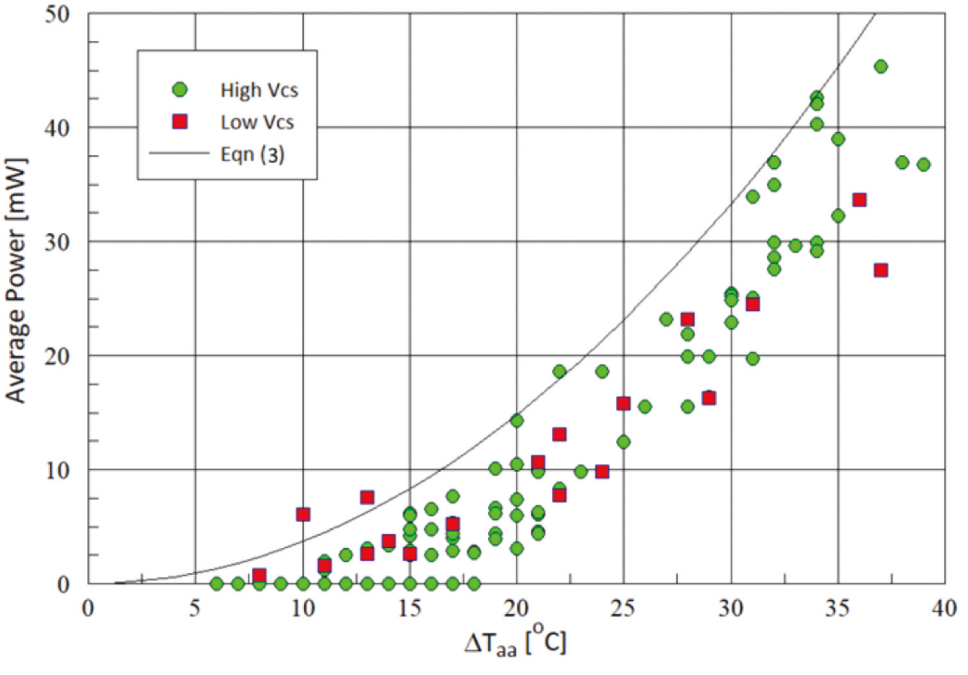

Figure 10. Power harvested versus measured temperature differential. The green circles are for the fixed-point electronics with V_{cs} = 0.9-V. The red squares are for the MPP electronics with V_{cs} = 0.1-V. The solid line is the energy available from the TEG according to Equation (3).

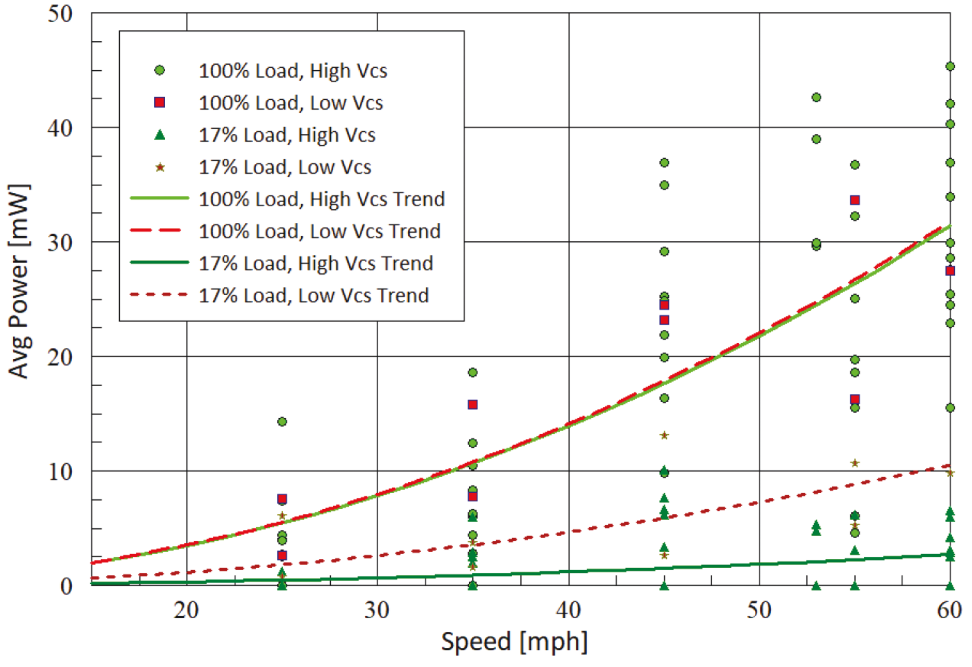

Figure 11. Power harvested versus speed for different loads. Light and dark green represent the high V_{cs} electronics at 100% load and 17% load, respectively. Light and dark red represent the low V_{cs} electronics.

4.4. Harvesting performance vs. speed and load

Figure 11 shows the power harvested versus speed and load. As in the previous graph, each point represents an average over one segment of one run. The solid lines are square law fits to each of the four subcategories (100% versus 17% load and high V_{cs} versus low V_{cs}).

Fully loaded conditions reliably produced enough temperature differential to ensure a cold start. For this reason, the 100% trend lines for the high V_{cs} and low V_{cs} circuits are almost identical. This indicates very similar conversion efficiencies. On the other hand, empty cars produce much lower differentials, and the 17% trend lines show significantly different performance for high and low V_{cs}. As stated earlier, this is due to the high V_{cs} circuit often producing no power at all when ΔT_{aa} is low.

4.5. Effect of wireless device

The amount of power consumed by a wireless monitoring device can easily vary over an order of magnitude depending on the communication protocol, the distance required, the amount of data captured, the amount of data transferred, and the frequency of data collection. One key factor is whether the wireless device has a receiver and whether it is powered at all times or only on a pre-arranged schedule. While the quantitative results in this section are specific only to this application, the results are useful to (a) determine if the intermittent nature of the current drawn by the device negatively impacts the performance of the TEG and conversion electronics and (b) demonstrate that the system can easily supply enough power for frequent on-demand monitoring of vibration spectra.

The BLE protocol used here can receive and respond to commands from a central hub with at most 100-ms latency and can therefore be considered ‘always on’. Data is acquired and transmitted whenever requested by the central hub. One question is what fraction of the power is essentially fixed devoted to monitoring the BLE, and what fraction is dependent on the amount of data

Table 7. An overall power consumption comparison between short (1-second) and long (4-second) bursts of accelerometer data acquired.

Burst Length [s]	Samples per Burst	Bytes per Burst	Collection Interval [s]	Minimum Power [mW]	Maximum Power [mW]	Average Power [mW]
1.0	5200	7.8k	600.0	1.31	3.68	**2.25**
4.0	20800	31.2k	600.0	1.33	4.18	**2.35**

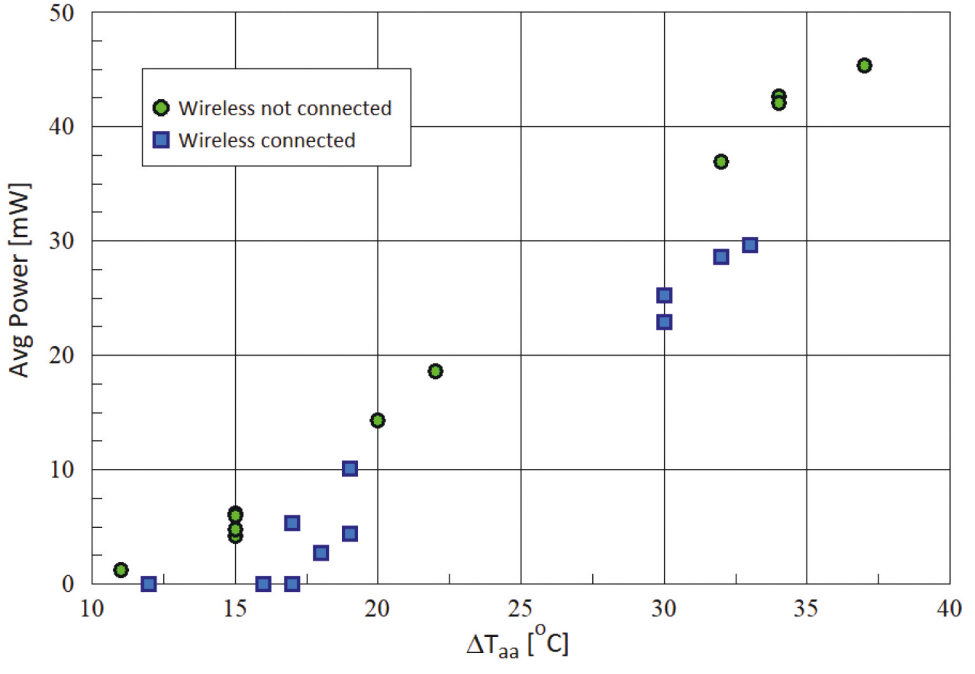

Figure 12. Power harvested with (blue) and without (green) wireless device connected. The vertical axis is total power produced by the boost converter, not power delivered to the battery, so the reduction cannot be attributed simply to power usage by the wireless.

requested. Table 7 compares overall power consumption with short (1-second) and long (4-second) bursts of accelerometer data acquired.

The results for the average power indicate that for this application, the fixed power consumption due to leaving on the BLE transceiver and its support microcontroller is strongly dominant. Even in the case of long bursts, 94% of the power is fixed and only 6% is due to the additional data collection.

It was found that having the wireless device directly connected to the battery did result in some deterioration of harvesting performance. Figure 12 shows a head-to-head comparison between Runs 1 + 3 (no wireless, green circles) and Runs 9 + 11 (wireless, 4-second data, blue squares). The vertical axis is the total power produced by the boost converter, not the power delivered to the battery, so the reduction cannot be attributed simply to power usage by the wireless. Instead, it appears that the intermittent high current draw of the wireless module causes temporary shutdowns of the boost converter. This would indicate that, in future designs, more care should be taken to isolate the converter from rapid variations in load, perhaps through the addition of an LC low pass filter between the battery and the wireless device.

5. Conclusions

This paper presented experimental results for a TEG harvesting system mounted on a railroad bearing adapter and powering a wireless bearing health monitoring device. The primary conclusions from this work follow:

- The harvesting system produces more than sufficient energy to power an always-on wireless monitoring device for an indefinite period of time, when used with a storage battery and operated over typical freight routes.
- Therefore, wireless bearing monitoring with no scheduled battery replacement and limited only by component lifetime is feasible.
- As expected, conversion with a low cold start voltage V_{cs} has a major advantage at low-temperature differentials, corresponding to low load and low speed. At higher temperature differentials, the advantage disappears. If there will be extended operation at low speeds and/or loads, it is essential to use a TEG with high $V_{oc}/\Delta T$ in combination with a boost converter that has a very low cold start voltage. However, the values required are well within the reach of commercially available components.

Acknowledgements

The authors want to acknowledge the National Science Foundation (NSF) CREST Center for Multidisciplinary Research Excellence in Cyber-Physical Infrastructure Systems (MECIS) and Hum Industrial Technology, Inc. for supporting this work. The authors also want to acknowledge the support provided by the University Transportation Center for Railway Safety (UTCRS) at UTRGV.

Disclosure statement

No potential conflict of interest was reported by the authors.

Funding

This study was made possible by funding provided by the NSF CREST MECIS through Award No. 2112650, and Hum Industrial Technology, Inc.

ORCID

Constantine Tarawneh http://orcid.org/0000-0002-4074-5627

References

[1] Federal Railroad Administration Safety Data [Internet] [Accessed 2021 June 5]https://safetydata.fra.dot.gov/officeofsafety/publicsite/query/inccaus.aspx
[2] TADS Trackside Acoustic Detection System [Internet] [Accessed 2021 June 5] https://aar.com/pdfs/TADSupdate_20160615.pdf
[3] Tarawneh C, Aranda J, Hernandez V, et al. An investigation into wayside hot-box detector efficacy and optimization. Int J of Rail Transportation. 2020;8(3):264–284.
[4] Tarawneh C, Aranda J, Hernandez V, et al. An analysis of the efficacy of wayside hot-box detector data. In: Proceedings of the 2018 ASME joint rail conference (JRC2018). Pittsburgh (PA); April 18–20, 2018, V001T02A012.
[5] Cuanang J, Tarawneh C, Amaro M, et al. Optimization of railroad bearing health monitoring system for wireless utilization. In: Proceedings of the 2020 ASME Joint Rail Conference (JRC2020). Virtual; April 20–22, 2020, V001T03A007.
[6] Hosseinkhani A, Younesian D, Eghbali P, et al. Sound and vibration energy harvesting for railway applications: a review on linear and nonlinear techniques. Energy Rep. 2021;7:852–874.

[7] Gao M, Wang P, Wang Y, et al. Self-powered ZigBee wireless sensor nodes for railway condition monitoring. IEEE Trans Intell Transp Syst. 2018;19(3):900–909.
[8] Gao M, Cong J, Xiao J, et al. Dynamic modeling and experimental investigation of self-powered sensor nodes for freight rail transport. Appl Energy. 2020;257:113969.
[9] Yazawa K, Bahk J-H, Shakouri A. Thermoelectric energy conversion devices and systems (WSPC Series in advanced integration and packaging). Singapore: World Scientific Publishing; 2020.
[10] Gao M, Su C, Cong J, et al. Harvesting thermoelectric energy from railway track. Energy. 2019;180 (C):315–329.
[11] Ahn D, Choi K. Performance evaluation of thermoelectric energy harvesting system on operating rolling stock. Micromach. 2018;9(7):359.
[12] C L III, Tarawneh C, Fuentes A, et al. Optimizing power consumption of freight railroad bearings using laboratory experimental data. In: Proceedings of the 2020 ASME joint rail conference (JRC2020). Virtual, April 20–22, 2020, V001T02A004.
[13] Arroyo J An experimentally validated finite element model of thermal transient response of a railroad bearing adapter. Master of Science in Engineering (MSE) Thesis, University of Texas Rio Grande Valley, May 2022.
[14] Witting I, Chasapis T, Ricci F, et al. The thermoelectric properties of bismuth telluride. Adv Electron Mater. 2019;5(6):1800904.
[15] E-peas, Inc. Datasheet for AEM20940 [Internet] [Accessed 2023 January 18] https://e-peas.com/e-peas_aem20940-datasheet-thermal-energy-harvesting/
[16] Tecteg. TEG2-126DLT datasheet [Internet] [Accessed 2023 January 18] https://thermoelectric-generator.com/wp-content/uploads/2017/10/TEG2-126LDT-Spec.-sheet.1.-REV.pdf
[17] 1A standalone linear li-ion battery charger with thermal regulation in SOP-8 Datasheet [Internet] [Accessed 2021 July 3]http://www.tp4056.com/d/tp4056.pdf
[18] Calc Maps [Internet] [Accessed 2021 July 3]https://www.calcmaps.com/map-distance
[19] Open Railway Map [Internet] [Accessed 2021 July 3]https://www.openrailwaymap.org/index.php
[20] Amaro M Developing a prototype energy harvesting device for powering wireless onboard condition monitoring sensor modules for railway service. Master of Science in Engineering (MSE) Thesis, University of Texas Rio Grande Valley, December 2021.
[21] Tarawneh C, Sotelo L, De Los Santos N, et al. Temperature profiles of railroad tapered bearings with defective inner and outer rings. Proceedings of the 2016 ASME joint rail conference (JRC 2016). Columbia, SC; April 12-15, 2016, V001T06A018.